Realistic Analytical Phantoms for Parallel Magnetic Resonance Imaging

M. Guerquin-Kern*, L. Lejeune, K. P. Pruessmann, and M. Unser

Abstract—The quantitative validation of reconstruction algorithms requires reliable data. Rasterized simulations are popular but they are tainted by an aliasing component that impacts the assessment of the performance of reconstruction. We introduce analytical simulation tools that are suited to parallel magnetic resonance imaging and allow one to build realistic phantoms. The proposed phantoms are composed of ellipses and regions with piecewise-polynomial boundaries, including spline contours, Bézier contours, and polygons. In addition, they take the channel sensitivity into account, for which we investigate two possible models. Our analytical formulations provide well-defined data in both the spatial and k-space domains. Our main contribution is the closed-form determination of the Fourier transforms that are involved. Experiments validate the proposed implementation. In a typical parallel magnetic resonance imaging reconstruction experiment, we quantify the bias in the overly optimistic results obtained with rasterized simulations—the inverse-crime situation. We provide a package that implements the different simulations and provide tools to guide the design of realistic phantoms.

Index Terms—Fourier analytical simulation, inverse crime, magnetic resonance imaging (MRI), Shepp–Logan.

I. INTRODUCTION

AN ACTIVE area of research in magnetic resonance imaging (MRI) is the development of reconstruction algorithms. In particular, the inverse-problem approach is getting popular [2], where one relies on an accurate model of the measurement process and possibly on additional information about the object being imaged.

In general, the development of any reconstruction approach requires that it be evaluated and compared to others. There are several reasons to rely on simulations in a first step:

- saving the costs inherent to getting real scanner data;
- testing the suitability of the implemented discrete forward model;

- quantitatively evaluating the performance of the reconstruction software;
- providing reliable ground-truth data to compare with.

However, for the results to be meaningful, simulations must be accomplished carefully. For instance, the inverse-crime situation, where exactly the same discrete model is used for simulation and reconstruction, leads to artificially good results. In the context of MRI, many developers of algorithms base their simulations on rasterized images. One should just be aware that such testing does not account for the full continuous-domain reality, because it neglects the aliasing that is inherent to spatial discretization. More realistic simulations are required to remove this bias and to ensure that the methods will perform adequately in practice.

A method to obtain resolution-independent simulations is to formulate the simulation analytically in the continuous domain. This approach goes back to Shepp and Logan [3], who introduced an ellipse-based phantom (SL) for X-ray tomography. For MRI, several analytical phantoms have been proposed. The first works, based on the SL phantom, are by Smith *et al.* [4], followed by Van de Walle *et al.* [5]. More recently, Koay *et al.* [6] worked out the MR contribution of an ellipsoid for the 3-D extension of the SL phantom. Gach *et al.* [7] adapted these elliptical phantoms specifically for MRI, introducing realistic physical parameters as well as T_1 and T_2 relaxation times. The family of analytical phantoms is extended by two recent works by Greengard and Stucchio [8] that use Gaussian functions, and Ngo *et al.* [9] that introduce 3-D polyhedra.

The attractiveness of currently known analytical phantoms is limited for two reasons. First, the vast majority of currently available phantoms (except [9]) use ellipses as basic elements. While such simple shapes have the advantage of mathematical tractability, they do not lend themselves well to the generation of images with realistic anatomical features. Secondly, to the best of our knowledge, no analytical phantom has been proposed that would take into account MRI receiving-coil sensitivities in the context of the simulation of parallel MRI experiments [10].

In this work, we extend the class of available analytical phantoms by introducing regions parameterized by spline contours which are general enough to reproduce polygons and Bézier contours. Our shapes are well suited for the description of realistic anatomical regions [11]. To accurately simulate image formation in parallel MRI, we also make use of analytical models for the coil sensitivity maps. Specifically, we investigate the use of two classes of basis functions—polynomials [10] and complex sinusoids—which both have the ability to generate maps that are physically realistic. These parametric forms are used to derive closed-form solutions for the MRI coil data. We have implemented and tested both models. Our conclusion is that the

TABLE I
GLOSSARY

Acronyms

(p)MR(I)	(Parallel) magnetic resonance (imaging)
FOV	Field of view
ROI	Region of interest
S(E)(N)R	Signal-to-(error) (noise) ratio
(N)(R)MSE	(Normalized) (root-)mean-squared error
(D)FT	(Discrete) Fourier transform
SL	Shepp-Logan
TV	Total variation
EPI	Echo planar imaging

Continuous Domain and Functions

$\mathbf{r}$	$\in \mathbb{R}^2$	spatial coordinates (XY plane)
$\mathbf{k}$	$\in \mathbb{R}^2$	k-space coordinates (XY plane)
$\boldsymbol{\omega}$	$\in \mathbb{R}^2$	Fourier angular frequency
$\rho(\mathbf{r})$	$\in \mathbb{R}^+$	object (proton density) in space
$m_S(\mathbf{k})$	$\in \mathbb{C}$	k-space observation from channel S
$S(\mathbf{r})$	$\in \mathbb{C}$	spatial sensitivity of the channel
$\hat{f}(\boldsymbol{\omega})$	$\in \mathbb{C}$	function f in the Fourier domain
$\mathbb{1}_{\mathcal{R}}(\mathbf{r})$	$\in \{0,1\}$	characteristic function of a region $\mathcal{R}$
$\partial \mathcal{R}$		contour of a region $\mathcal{R}$
J_n	$\in \mathbb{R}^{\mathbb{R}}$	n-th order Bessel function of the first kind
erf	$\in \mathbb{C}^{\mathbb{C}}$	error function of a complex argument
$\gamma(s,z)$	$\in \mathbb{C}^{\mathbb{R} \times \mathbb{C}}$	lower incomplete gamma function

Discrete Data and Linear Algebra

$\mathbf{X}^{\mathrm{T}}$		transpose of the matrix $\mathbf{X}$
$\mathbf{x}.\mathbf{y}$	$\in \mathbb{R}$	regular inner product
$\mathbf{e}_i$	$\in \mathbb{R}^d$	the canonical vectors such that $\mathbf{x}.\mathbf{e}_i = x_i$
$\delta_{k,l}$	$\in \{0,1\}$	Kronecker's delta (1 if $k=l$ and 0 otherwise)
j	$\in \mathbb{C}$	imaginary unit such that $\mathrm{j}^2 = -1$

Multi-Index Notations for $\boldsymbol{\alpha} \in \mathbb{N}^d$

$\mathbf{z}^{\boldsymbol{\alpha}}$	$=$	$\prod z_i^{\alpha_i}$	$\in \mathbb{R}$
$|\boldsymbol{\alpha}|$	$=$	$\sum \alpha_i$	$\in \mathbb{N}$
$\mathbf{p}!$	$=$	$\prod p_i!$	$\in \mathbb{N}$
$\binom{\mathbf{p}}{\mathbf{q}}$	$=$	$\prod \binom{p_i}{q_i} = \frac{\mathbf{p}!}{(\mathbf{p}-\mathbf{q})!\mathbf{q}!}$	$\in \mathbb{N}$
$\sum_{\mathbf{p}=\mathbf{a}}^{\mathbf{b}}$	$=$	$\sum_{p_1=a_1}^{b_1} \sum_{p_2=a_2}^{b_2} \cdots$	

new sinusoidal one is preferable because it is better conditioned and robust to roundoff errors, while offering of the modeling flexibility that is required. The polynomial model works well with ellipses and polygons, but tends to display numerical instabilities with Bézier contours when the order becomes too high.

This document is organized as follows. In Section II, we present the different models considered for the parallel MRI measurement process, the analytical phantom, and the coil sensitivities. We motivate and compare the polynomial and the proposed sinusoidal models. In Section III, we propose the main theoretical elements that make the analytical MRI simulation possible, deferring the more technical considerations until the Appendix. Finally, we present in Section IV the experiments that validate our implementation of the theoretical tools and an application that quantifies the bias of rasterized simulations on linear and nonlinear reconstructions, in a typical parallel MRI setup.

II. MODELING

In this section, we present the MRI measurement model and building blocks that are used to define our phantom. The main notations adopted are summarized in Table I.

A. Parallel MRI

We use the well-established linear model for parallel MRI that relates the object ρ to the k-space signal m_{S_n} observed by each receiving coil, via the Fourier integral

$$m_{S_n}(\mathbf{k}) = \int S_n(\mathbf{r})\rho(\mathbf{r})e^{\mathrm{j}2\pi\mathbf{k}\cdot\mathbf{r}}\mathrm{d}\mathbf{r} \qquad (1)$$

where S_n accounts for the sensitivity map of the nth receiving channel. The sensitivity map is defined as $S_n(\mathbf{r}) = B_x(\mathbf{r}) - \mathrm{j}B_y(\mathbf{r})$, where, by the principle of reciprocity, $\mathbf{B}(\mathbf{r}) = (B_x(\mathbf{r}), B_y(\mathbf{r}), B_z(\mathbf{r}))$ corresponds to the magnetic field generated at point $\mathbf{r}$ by a unit-value steady current in the coil. The Biot–Savart law relates this field to the coil geometry through the relation

$$\mathbf{B}(\mathbf{r}) \propto \oint_{\mathrm{coil}} \frac{\mathrm{d}\mathbf{u} \times (\mathbf{u} - \mathbf{r})}{\|\mathbf{u} - \mathbf{r}\|^3}. \qquad (2)$$

B. Analytical Phantom

We mathematically define the phantom ρ as a simple function, involving R regions $\mathcal{R}_i$ of constant intensity ρ_i

$$\rho(\mathbf{r}) = \sum_{i=1}^{R} \rho_i \mathbb{1}_{\mathcal{R}_i}(\mathbf{r}). \qquad (3)$$

The term *region* refers to a connected and bounded set. The symbol $\mathbb{1}_{\mathcal{R}}$ denotes the characteristic function of a region $\mathcal{R}$. Such a phantom has a limited spatial support ($\bigcup_{i=1}^{R} \mathcal{R}_i$) that we call a *region of interest* (ROI).

This model allows us to render realistic phantoms of two kinds

- piecewise-constant phantoms that mimic segmented data with sharp contours (e.g., the SL brain phantom);
- textured phantom via a triangular-mesh approach.

We investigate the first approach in this paper. The contours that are considered are ellipses, polygons, and quadratic-spline curves. We show in Fig. 1 three such phantoms that we use in our experiments.

C. Sensitivity Models

For computations, we need to parameterize the complex sensitivity maps. It is commonly admitted that they are smooth and slowly-varying spatially. It is therefore possible to generate physically-realistic sensitivity maps using a reasonably small number of lowpass basis functions. Here, we discuss two models that are well-suited for this task. They both relate linearly the parameters to the complex sensitivity values. Moreover, their corresponding MRI models involve the Fourier integrals of monomials over the regions of the phantom.

Definition II-1: For $\boldsymbol{\alpha} \in \mathbb{N}^d$ and $\mathcal{R}$ a region of $\mathbb{R}^d$

$$f_{\mathcal{R}}^{\boldsymbol{\alpha}}(\boldsymbol{\omega}) = \int_{\mathcal{R}} \mathbf{r}^{\boldsymbol{\alpha}} e^{-\mathrm{j}\boldsymbol{\omega}\cdot\mathbf{r}}\mathrm{d}\mathbf{r}. \qquad (4)$$

Here, we adopted the multi-index notation $\mathbf{r}^{\boldsymbol{\alpha}}$ defined in Table I.

1) Polynomial Sensitivity: This model, first proposed in [10] to represent the local behavior of the sensitivity, assumes that the coil sensitivity S is represented by a polynomial of degree

Fig. 1. Phantoms parameterized by elliptical and Bézier-defined regions. From left to right: rectangle phantom used for validation, the Shepp–Logan phantom, and a proposed brain phantom. The PDF and SVG versions of these phantoms are available online at http://bigwww.epfl.ch/algorithms/mriphantom/.
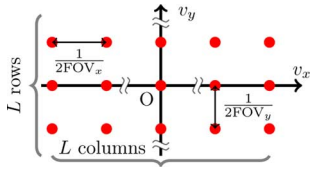

Fig. 2. Grid of the angular frequencies involved in the sinusoidal model.

D inside the ROI as

$$S(\mathbf{r}) = \sum_{d=0}^{D} \sum_{|\boldsymbol{\alpha}|=d} s_{d,\boldsymbol{\alpha}} \mathbf{r}^{\boldsymbol{\alpha}}, \quad \forall \, \mathbf{r} \in \text{ROI}. \quad (5)$$

As the degree D increases, the model will reproduce sharper transitions. The number of polynomial coefficients is $N_p = (D+1)(D+2)/2$.

The corresponding MR response is given by

$$m_S(\mathbf{k}) = \sum_{i=1}^{R} \rho_i \sum_{d=0}^{D} \sum_{|\boldsymbol{\alpha}|=d} s_{d,\boldsymbol{\alpha}} f_{\mathcal{R}_i}^{\boldsymbol{\alpha}}(-2\pi\mathbf{k}). \quad (6)$$

2) Sinusoidal Sensitivity: Alternatively, the coil sensitivity is defined by the linear combination of complex exponentials

$$S(\mathbf{r}) = \sum_{\mathbf{v}} s_{\mathbf{v}} e^{j\mathbf{r}\cdot\mathbf{v}}, \quad \forall \, \mathbf{r} \in \text{ROI}. \quad (7)$$

We propose to constrain the problem to the angular frequencies $\mathbf{v}$ on a Cartesian grid with spacings that correspond to twice the considered field-of-view (FOV). The low-frequency properties are ensured by only considering the $L \times L$ angular frequencies around the origin (see Fig. 2).

Similarly to the effect of the polynomial degree D, an increase in the parameter L allows one to reproduce sharper transitions. The number of coefficients is given by $N_s = L^2$. The corresponding MR response is given by

$$m_S(\mathbf{k}) = \sum_{i=1}^{R} \rho_i \sum_{\mathbf{v}} s_{\mathbf{v}} f_{\mathcal{R}_i}^{\mathbf{0}}(-2\pi\mathbf{k} - \mathbf{v}). \quad (8)$$

3) Comparison: In order to evaluate and compare the ability of the two models to describe realistic sensitivity maps, we considered a 256×256 rasterization of the SL phantom and the

27 648 pixels of its ROI. Using Biot–Savart's law (2), we simulated the complex sensitivity maps of a 24-channel circular head coil array (FOV = 28 cm, distance to center = 17 cm, radius = 5 cm) distributed around the phantom. Then, the parameters of the two models where selected to fit the maps. In Fig. 3, the average fitting properties of the two models are presented as a function of the number of parameters.

We observe that the fitting accuracy of both models rapidly increases with the number of parameters, with a sensible advantage for the sinusoidal model. The downside is an increased condition number for the fitting operations. With respect to that criterion, the sinusoidal model behaves also better. The maximal spatial errors are comparable for both models.

III. ANALYTICAL MRI MEASUREMENTS

A. Overview of Analytical Fourier Computations

In this section, we present the theoretical tools that are necessary to derive the analytical expression of the MRI measurements. Proofs and additional calculation details are provided in the Appendix.

The models presented in the previous section allow us to decompose the analytical MRI measurements into Fourier integrals of the sensitivity over the regions that compose the phantom. Depending on the type of region or sensitivity model, we propose tailored methods to decompose the analytical response as a sum of special functions that can be computed accurately and rapidly. In Fig. 4, we present the roadmap of these decompositions that are defined and worked out in the sequel.

B. Elliptical Regions

Let us consider an elliptical region $\mathcal{E}$ parameterized by its center $\mathbf{r}_c$, the angle θ formed between its semimajor axis A and the abscissa, and its semiminor axis B. The linear transformation

$$\mathbf{r} \mapsto \mathbf{u} = \mathbf{D}^{-1}\mathbf{R}^{\text{T}}(\mathbf{r} - \mathbf{r}_c) \quad (9)$$

with $\mathbf{D} = \text{diag}(A, B)$ and $\mathbf{R}$ the rotation matrix of angle θ, maps $\mathcal{E}$ into a unit disk, that is to say, $\mathcal{E} = \{\mathbf{u} \mid \|\mathbf{u}\| \leq 1\}$. The Fourier transform of the unit disk involves the functions

$$G_n(\mathbf{x}) = \frac{J_n(\|\mathbf{x}\|)}{\|\mathbf{x}\|^n} \quad (10)$$
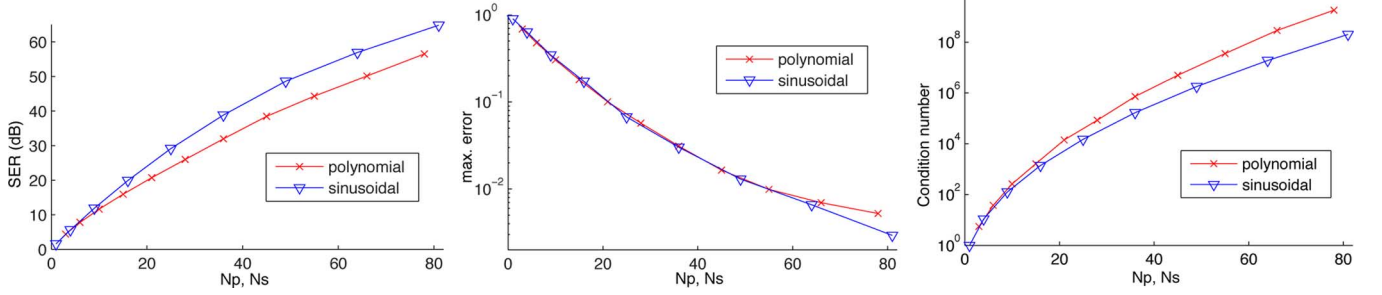
Fig. 3. Fitting properties of the two sensitivity models as a function of the number of parameters. From left to right: approximation SER in dB, maximal absolute error, and condition number of the fitting matrix.
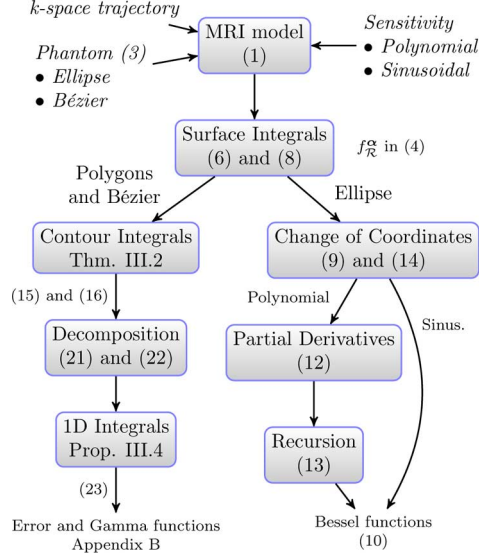

Fig. 4. Roadmap of analytical Fourier computations.

where J_n denotes the nth-order Bessel function of the first kind [12].

Using the sinusoidal sensitivity model, the integral $f_{\mathcal{E}}^0$ can be worked out [5] as

$$f_{\mathcal{E}}^{\mathbf{0}}(\boldsymbol{\omega}) = 2\pi|\mathbf{D}|e^{-j\boldsymbol{\omega}\cdot\mathbf{r}_c}G_1\left(\mathbf{D}\mathbf{R}^{\mathrm{T}}\boldsymbol{\omega}\right) \tag{11}$$

where $|\mathbf{D}|$ represents the absolute value of the determinant of matrix $\mathbf{D}$.

When considering the polynomial sensitivity model, we suggest to first consider the change of variables (9), rather than computing $f_{\mathcal{E}}^{\boldsymbol{\alpha}}$ directly. We write that

$$\int_{\mathcal{E}}\mathbf{u}^{\boldsymbol{\alpha}}e^{-j\boldsymbol{\omega}\cdot\mathbf{r}}d\mathbf{r} = 2\pi|\mathbf{D}|j^{|\boldsymbol{\alpha}|}e^{-j\boldsymbol{\omega}\cdot\mathbf{r}_c}\left(\frac{\partial^{|\boldsymbol{\alpha}|}G_1}{\partial\mathbf{x}^{\boldsymbol{\alpha}}}\right)\left(\mathbf{D}\mathbf{R}^{\mathrm{T}}\boldsymbol{\omega}\right). \tag{12}$$

The interesting point is that the partial derivatives $\partial^{|\boldsymbol{\alpha}|}G_1/\partial\mathbf{x}^{\boldsymbol{\alpha}}$ can be decomposed recursively as a sum of G_n thanks to the property

$$\nabla G_n(\mathbf{x}) = -\mathbf{x}G_{n+1}(\mathbf{x}). \tag{13}$$

The coefficients of the polynomial in terms of the new coordinates (9) are required to satisfy

$$S(\mathbf{r}) = \sum_{d=0}^{D}\sum_{|\boldsymbol{\alpha}|=d}s_{d,\boldsymbol{\alpha}}\mathbf{r}^{\boldsymbol{\alpha}} = \sum_{d=0}^{D}\sum_{|\boldsymbol{\alpha}|=d}t_{d,\boldsymbol{\alpha}}\mathbf{u}^{\boldsymbol{\alpha}}. \tag{14}$$

They can be computed by inverting the matrix that relates the N_p coefficients to the sensitivity values at $N \geq N_p$ randomly chosen points in terms of the new coordinates.

The MR contribution of such an elliptical contour is presented in Table II.

C. Piecewise-Quadratic Contours

In this section, we first provide relations for the computation of the d-dimensional Fourier transform of a monomial delimited by a connected subset $\mathcal{B}$ of $\mathbb{R}^d$. With methods that are similar to the ones used in [13], we show how to decompose the d-dimensional Fourier integral into a sum of integrals over the contour $\partial\mathcal{B}$. These summed integrals are of reduced dimensionality. In a second step, we show how quadratic-spline curves involve a family of 1-D integrals.

1) Fourier Transform of Monomials Over a Connected Set: We show that the surface integral $f_{\mathcal{B}}^{\boldsymbol{\alpha}}$ in (4) can be decomposed into a sum of contour integrals.

Definition III-1: We define

$$g_{\mathcal{B}}^{\boldsymbol{\alpha}}(\mathbf{0}) = \int_{\partial\mathcal{B}}\frac{\mathbf{r}^{\boldsymbol{\alpha}+\mathbf{e}_k}}{1+\alpha_k}\mathbf{e}_k\cdot\mathbf{n}d\sigma, \quad \text{for any } k \tag{15}$$

$$g_{\mathcal{B}}^{\boldsymbol{\alpha}}(\boldsymbol{\omega}) = \int_{\partial\mathcal{B}}\mathbf{r}^{\boldsymbol{\alpha}}\frac{e^{-j\boldsymbol{\omega}\cdot\mathbf{r}}}{\|\boldsymbol{\omega}\|^2}\boldsymbol{\omega}\cdot\mathbf{n}d\sigma, \quad \forall\boldsymbol{\omega}\in\mathbb{R}^d\setminus\{\mathbf{0}\} \tag{16}$$

where $\mathbf{n}$ stands for the outward-pointing unit normal of boundary element $d\sigma$. Note that $g_{\mathcal{B}}^{\boldsymbol{\alpha}}$ is not continuous at the origin $\boldsymbol{\omega} = \mathbf{0}$.

Theorem III-2: For $\boldsymbol{\omega}\in\mathbb{R}^d\setminus\{\mathbf{0}\}$ and $\boldsymbol{\alpha}\in\mathbb{N}^d$

$$f_{\mathcal{B}}^{\boldsymbol{\alpha}}(\boldsymbol{\omega}) = j\sum_{\mathbf{m}=0}^{\boldsymbol{\alpha}}\left(\frac{-j\boldsymbol{\omega}}{\|\boldsymbol{\omega}\|^2}\right)^{\boldsymbol{\alpha}-\mathbf{m}}|\boldsymbol{\alpha}-\mathbf{m}|!\binom{\boldsymbol{\alpha}}{\mathbf{m}}g_{\mathcal{B}}^{\mathbf{m}}(\boldsymbol{\omega}) \tag{17}$$

and

$$f_{\mathcal{B}}^{\boldsymbol{\alpha}}(\mathbf{0}) = g_{\mathcal{B}}^{\boldsymbol{\alpha}}(\mathbf{0}). \tag{18}$$

The consequence of Theorem III-2 is that the d-dimensional integral $f_{\mathcal{B}}^{\boldsymbol{\alpha}}$ can be decomposed into a sum of $(d-1)$-dimensional integrals. By recursion, the $f_{\mathcal{B}}^{\boldsymbol{\alpha}}$ can be computed via 1-D integrals. The proof is provided in Appendix A.

Note that the case $\boldsymbol{\omega} = \mathbf{0}$, which corresponds to the calculation of the moments of the region, has been worked out first by Jacob *et al.* in [14] for parametric 2-D spline contours.

2) Parameterization of a Contour in 2-D: The region $\mathcal{B}$ is defined by its boundary, the contour $\partial\mathcal{B}$. In 2-D, a convenient

TABLE II
CLOSED-FORM MR CONTRIBUTION OF ELLIPTICAL AND QUADRATIC BÉZIER REGIONS FOR THE PROPOSED SENSITIVITY MODELS

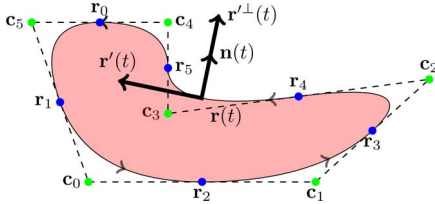| Sensitivity model	Ellipse	Quadratic Bézier curve
Sinusoidal (7)	$2\pi|\mathbf{D}|e^{j2\pi\mathbf{k}\cdot\mathbf{r}_c} \sum_{\mathbf{v}} s_{\mathbf{v}} e^{j\mathbf{v}\cdot\mathbf{r}_c} G_1\left(\mathbf{DR}(-\theta)(2\pi\mathbf{k}+\mathbf{v})\right)$	$\sum_{\mathbf{v}} s_{\mathbf{v}} f_{\mathcal{B}}^{\mathbf{0}}(-2\pi\mathbf{k}-\mathbf{v})$
Polynomial (14)	$2\pi|\mathbf{D}|e^{2\pi j\mathbf{k}\cdot\mathbf{r}_c} \sum_{d=0}^{D} \sum_{|\boldsymbol{\alpha}|=d} j^{|\boldsymbol{\alpha}|} t_{d,\boldsymbol{\alpha}} \frac{\partial^{|\boldsymbol{\alpha}|} G_1}{\partial\mathbf{x}^{\boldsymbol{\alpha}}} (2\pi\mathbf{DR}(-\theta)\mathbf{k})$	$\sum_{d=0}^{D} \sum_{|\boldsymbol{\alpha}|=d} s_{d,\boldsymbol{\alpha}} f_{\mathcal{B}}^{\boldsymbol{\alpha}}(-2\pi\mathbf{k})$

Fig. 5. Example of a quadratic-spline-defined region with $N = 6$ control points. The boundary is described counter-clockwise and the normal vector is outward-pointing. The contour is represented piecewise by quadratic Bézier curves.

way to parameterize the contour is by the use of a B-spline generating function φ such that

$$\forall\, \mathbf{r} \in \partial\mathcal{B}, \exists t \in \mathbb{R}, \quad \mathbf{r}(t) = \sum_{p \in \mathbb{Z}} \mathbf{c}_p \varphi(t-p). \quad (19)$$

The considered contour is closed. Consequently, the vector-valued function $\mathbf{r}$ must be periodic. In addition, the number N of coefficients $\mathbf{c}_p$ that characterize the curve must be finite. The simplest way to satisfy these constraints is to impose that the sequence of coefficients $\mathbf{c}_p$ be N-periodic. This enforces the N-periodicity of $\mathbf{r}$.

If we note φ_p the N-periodized version of φ, the contour is parameterized either globally as

$$\forall\, t \in [0,N], \quad \mathbf{r}(t) = \sum_{q=0}^{N-1} \mathbf{c}_q \varphi_p(t-q) \quad (20)$$

or piecewise, with $0 \le t = n + \lambda < M$, $n \in 0\ldots N-1$ and $\lambda \in [0,1]$, as

$$\mathbf{r}(\lambda+n) = \sum_{q=0}^{N-1} \mathbf{c}_{n-q} \varphi_p(\lambda+q). \quad (21)$$

3) Decomposition of the Contour Integrals: We introduce the notation $\mathbf{z}^{\perp}$ for the vector perpendicular to $\mathbf{z}$ with same norm and pointing outwards the region $\mathcal{B}$ at the considered point (see Fig. 5). We write $\mathbf{r}'(t) = \partial\mathbf{r}/\partial t(t)$. The piecewise representation of the contour (21) can be exploited to decompose the contour integral of interest, for instance (15) or (16), which leads to

$$\int_{\partial\mathcal{B}} \mathbf{F}(\mathbf{r}) \cdot \mathbf{n} d\sigma = \sum_{q=0}^{N-1} \int_0^1 \mathbf{F}\left(\mathbf{r}(q+\lambda)\right) \cdot \mathbf{r}'^{\perp}(q+\lambda) d\lambda. \quad (22)$$

4) Quadratic Bézier Curves: In the sequel, we focus on contours represented by linear and quadratic B-splines. The former describe polygons while the latter give a piecewise description

of quadratic Bézier curves. Three equivalent piecewise representations can be useful and are given in Table III with their relationships.

Definition III-3:

$$h^{(m)}(a,b) = \int_0^1 \lambda^m e^{-j\lambda(a+\lambda b)} d\lambda. \quad (23)$$

Proposition III-4: For $\boldsymbol{\omega} \in \mathbb{R}^d \setminus \{\mathbf{0}\}$ and a contour $\partial\mathcal{B}$ parameterized piecewise by $\mathbf{r}(\lambda+n) = \mathbf{r}_n + \lambda\boldsymbol{\beta}_n + \lambda^2\boldsymbol{\gamma}_n$, with $n \in \mathbb{N}$ and $\lambda \in [0,1]$, we have that

$$g_{\mathcal{B}}^{\boldsymbol{\alpha}}(\boldsymbol{\omega}) = \sum_{n=0}^{N-1} e^{-j\boldsymbol{\omega}\cdot\mathbf{r}_n} \sum_{i=0}^{2|\boldsymbol{\alpha}|+1} d_{n,i} h^{(i)}(\boldsymbol{\omega}\cdot\boldsymbol{\beta}_n, \boldsymbol{\omega}\cdot\boldsymbol{\gamma}_n) \quad (24)$$

while

$$g_{\mathcal{B}}^{\boldsymbol{\alpha}}(\mathbf{0}) = \sum_{n=0}^{N-1} \sum_{i=0}^{2|\boldsymbol{\alpha}|+3} d'_{n,i} h^{(i)}(0,0) \quad (25)$$

where, with the notation $\sigma_{\mathbf{p}} = |\mathbf{p}_2| + 2|\mathbf{p}_3|$, the symbol $d_{n,i}$ stands for

$$\sum_{\mathbf{p}_1+\mathbf{p}_2+\mathbf{p}_3=\boldsymbol{\alpha}} \frac{\mathbf{r}_n^{\mathbf{p}_1} \boldsymbol{\beta}_n^{\mathbf{p}_2} \boldsymbol{\gamma}_n^{\mathbf{p}_3} \boldsymbol{\alpha}!}{\mathbf{p}_1!\mathbf{p}_2!\mathbf{p}_3!} \boldsymbol{\omega}\cdot\left(\boldsymbol{\beta}_n^{\perp}\delta_{\sigma_{\mathbf{p}},i} + 2\boldsymbol{\gamma}_n^{\perp}\delta_{\sigma_{\mathbf{p}},i-1}\right) \quad (26)$$

and $d'_{n,i}$ stands for

$$\sum_{\mathbf{p}_1+\mathbf{p}_2+\mathbf{p}_3=\boldsymbol{\alpha}+\mathbf{e}_k} \frac{\mathbf{r}_n^{\mathbf{p}_1} \boldsymbol{\beta}_n^{\mathbf{p}_2} \boldsymbol{\gamma}_n^{\mathbf{p}_3} \boldsymbol{\alpha}!}{\mathbf{p}_1!\mathbf{p}_2!\mathbf{p}_3!} \mathbf{e}_k\cdot\left(\boldsymbol{\beta}_n^{\perp}\delta_{\sigma_{\mathbf{p}},i} + 2\boldsymbol{\gamma}_n^{\perp}\delta_{\sigma_{\mathbf{p}},i-1}\right). \quad (27)$$

The values $h^{(m)}(a,b)$ follow a three-term recurrence relation [15]. More details on their numerical computation are given in Appendix B.

Note that the piecewise parameterization of the contour of a polygon corresponds to the particular case of a quadratic parameterization with $\boldsymbol{\beta}_n = \mathbf{r}_{n+1} - \mathbf{r}_n$ and $\boldsymbol{\gamma}_n = \mathbf{0}$. Such simpler polygonal models with homogeneous sensitivities have been considered in prior work [8, Prop. 3.2] using a similar formulation.

IV. EXPERIMENTS

A. Implementation Details

Our implementation uses Matlab 7.12 (Mathworks, Natick, MA). The experiments run on a 64-bit 8-core computer, 8 GB RAM, Mac OS X 10.6.7.

We implemented the analytical computations as described by the scheme in Fig. 4, with double float precision. For efficient computations of the error function of a complex variable, we

TABLE III
PIECEWISE REPRESENTATIONS OF QUADRATIC-B-SPLINE CONTOURS

Representation	$\mathbf{r}(t) = \mathbf{r}(\lambda + n)$ with $n \in \mathbb{N}$ and $\lambda \in [0,1]$	Relations
B-spline (global)	$\frac{\lambda^2}{2}\mathbf{c}_n + \left(\frac{1}{2} + \lambda - \lambda^2\right)\mathbf{c}_{n-1} + \frac{1}{2}(1-\lambda)^2\mathbf{c}_{n-2}$	$\mathbf{r}_n = \frac{1}{2}\left(\mathbf{c}_{n-1} + \mathbf{c}_{n-2}\right)$
Polynomial (piecewise)	$\mathbf{r}_n + \lambda\boldsymbol{\beta}_n + \lambda^2\boldsymbol{\gamma}_n$	$\boldsymbol{\beta}_n = 2\left(\mathbf{c}_{n-1} - \mathbf{r}_n\right)$
Bézier curve (design)	$(1-\lambda)^2\mathbf{r}_n + 2\lambda(1-\lambda)\mathbf{c}_{n-1} + \lambda^2\mathbf{r}_{n+1}$	$\boldsymbol{\gamma}_n = \mathbf{r}_{n+1} + \mathbf{r}_n - 2\mathbf{c}_{n-1}$

coded the critical parts of `erfz` in C++/MEX, with POSIX multithreading, following Marcel Leutenegger's recommendations.[1] The code implementing Theorem III-2 utilizes Matt Fig's `npermutek`.[2] The rasterization of spline-defined regions, which is performed without approximation, partly relies on Bruno Luong's fast MEX implementation of `insidepoly`.[3] Our package also includes graphical tools to design the analytical phantoms. For purposes of adequate visualization, export to the popular vector-graphics formats SVG 1.1 and PDF (via the PGF/Tikz LATEX package) is supported. The package is distributed[4] in order to provide sensitivity fitting, phantom–design interface, analytical simulation tools, and to allow replication of the experiments of this section.

Unlike the sinusoidal model which is very robust to numerical errors, our current implementation of the three-term recurrence relation (see Appendix B) leads to instabilities when using the polynomial model. The theoretical relation $|h^{(m)}(a,b)| \leq 1/(m+1)$ is sometimes violated for orders $m \geq 2$ and large values of the first argument. This prevented us to present valid simulations of piecewise quadratic contours combined with a polynomial sensitivity. Given the comparison of the two models in Section II-C3, we considered the sinusoidal model with parameter $L = 7$, that is $N_s = 49$ in Fig. 3, which lead to accurate representations of the physical sensitivities and numerically tractable inversions.

As an alternative to our analytical method, we consider the traditional simulation procedure that consists in 1) sampling the phantom with a grid of a given size and 2) resampling the DFT of this discrete image according to the desired k-space trajectory. We call this procedure a rasterized simulation. It is expected to be consistent with our analytical method only when considering an infinitely dense sampling.

For reconstructions, we consider an optimization problem of the form

$$\mathbf{x}^\star = \arg\min_{\mathbf{x}} \|\mathbf{m} - \mathbf{E}\mathbf{x}\|_2^2 + \lambda\mathcal{P}(\mathbf{x}) \tag{28}$$

where $\mathbf{x}$ represents an image, $\mathbf{x}^\star$ is the reconstructed one, $\mathbf{m}$ is the concatenated scanner data vector, $\mathbf{E}$ is the encoding matrix, and $\mathcal{P}$ is a regularization function. With N receiving channels and M k-space measurements at positions $\{\mathbf{k}_m\}_{m=1\cdots M}$, the MRI encoding matrix $\mathbf{E}$ is formed as

$$\mathbf{E} = (\mathbf{I}_n \otimes \mathbf{E}_0)\left[\text{diag}\left(\mathbf{s}_1\right), \ldots, \text{diag}\left(\mathbf{s}_N\right)\right]^{\mathrm{T}} \tag{29}$$

TABLE IV
ERRORS OF OUR ANALYTICAL SIMULATIONS FOR THE RECTANGLE

NRMSE	1.5e-15
max. error in k-space	2.8e-16
max. error inverse DFT	7.0e-15

with $\mathbf{I}_n$ representing the $n \times n$ identity matrix, the symbol $\otimes$ standing for the Kronecker product, and $\mathbf{s}_n$ being the nth coil sensitivity map vector in the same way as $\mathbf{x}$. The encoding matrix $\mathbf{E}_0$ corresponds to the same MRI scan with a single homogeneous receiving coil and is defined as

$$\mathbf{E}_0 = [\mathbf{v}_1, \ldots, \mathbf{v}_M]^{\mathrm{T}}. \tag{30}$$

There, $\mathbf{v}_m$ are vectors such that, for a pixel of coordinates $\mathbf{p}$, $(\mathbf{v}_m)_{\mathbf{p}} = \exp\left(-2\mathrm{j}\pi\mathbf{k}_m \cdot \mathbf{p}\right)$.

We used two types of regularizations in our experiments.
- $\mathcal{P}(\mathbf{x}) = \|\mathbf{x}\|_2^2$ corresponds to a Tikhonov regularization, which leads to linear reconstructions that we implemented with the conjugate-gradient method.
- $\mathcal{P}(\mathbf{x}) = \|\mathbf{x}\|_{\mathrm{TV}}$ is the isotropic total-variation pseudo-norm, which leads to a nonlinear reconstruction problem. This reconstruction scheme is often used in compressed-sensing research and is particularly suited for dealing with piecewise-constant images such as our phantoms. We implemented it using the iteratively reweighted least-squares algorithm, also known as the additive form of the half-quadratic minimization [16], [17].

B. Validation of the Implementation

1) Simple Example With Homogeneous Sensitivity: As first validation, we consider the simple phantom composed of a rectangular region that is represented in Fig. 1. Under a proper change of variables, it yields a square and its Fourier transform is given by a product of sinc functions. This phantom is composed of a polygon and consequently falls in the category of the spline-defined contours. We test the accuracy of our proposed simulation method and of the rasterized approach against the closed-form solution. To do so, we consider the MR response associated with a homogeneous receiving coil sensitivity and a 256×256 Cartesian k-space sampling. The simulation errors are reported in Tables IV and V.

As expected, the error of rasterized simulations decreases when the sampling density increases. Meanwhile, the accuracy of our analytical implementation is as good as the machine `double float` precision would allow. Thus, we conclude that we can indistinctly use the closed-form ground truth or our proposed analytical model in the conditions of Section IV-BI.

2) Validation With Nonhomogeneous Sensitivity: We now use our analytical phantom as a gold standard to evaluate the accuracy the measurements obtained from rasterized simulations.

TABLE V
ERRORS OF THE RASTERIZED SIMULATIONS FOR THE RECTANGLE PHANTOM

Sampling density	256	352	400	512	704	800	1024	1408	1600	2048
NRMSE	5.58e-02	2.51e-02	2.01e-02	1.25e-02	7.45e-03	6.04e-03	3.85e-03	1.59e-03	1.27e-03	8.32e-04
max. error in k-space	5.5e-03	2.0e-03	1.5e-03	1.1e-03	5.5e-04	5.3e-04	3.6e-04	1.2e-04	1.0e-04	5.8e-05
max. error inverse DFT	5.5e-01	1.9e-01	1.6e-01	1.0e-01	6.2e-02	5.4e-02	3.9e-02	1.5e-02	1.2e-02	6.7e-03

TABLE VI
ERRORS OF THE RASTERIZED SIMULATIONS FOR THE BRAIN AND SL PHANTOMS VERSUS OUR ANALYTICAL SIMULATIONS

	Sampling density	128	176	256	352	512	704	1024	1408	2048	2816
Brain	NRMSE	1.45e-01	9.26e-02	5.45e-02	3.48e-02	2.13e-02	1.02e-02	6.70e-03	4.06e-03	2.03e-03	1.49e-03
	max. err. k-space	1.1e-02	5.7e-03	3.3e-03	2.6e-03	1.4e-03	6.6e-04	4.1e-04	2.4e-04	1.5e-04	9.5e-05
	max. err. inverse DFT	2.3e-01	1.4e-01	1.1e-01	7.9e-02	5.1e-02	2.0e-02	2.1e-02	1.4e-02	4.8e-03	5.6e-03
SL	NRMSE	2.76e-01	1.79e-01	9.74e-02	5.38e-02	2.85e-02	2.01e-02	1.28e-02	6.23e-03	3.34e-03	2.03e-03
	max. err. k-space	2.9e-02	1.6e-02	8.8e-03	4.9e-03	2.6e-03	1.7e-03	1.0e-03	6.1e-04	3.0e-04	1.7e-04
	max. err. inverse DFT	4.7e-01	3.0e-01	1.6e-01	1.1e-01	6.5e-02	3.9e-02	3.3e-02	1.3e-02	7.0e-03	5.0e-03

We consider the SL and brain phantoms. The single sensitivity map is computed using Biot–Savart's law and is approximated on the support of each phantom with the sinusoidal model. The k-space is on a 128×128 Cartesian grid. Errors are reported in Table VI.

We observe that the errors decrease with the same trend as in the rectangle case, which strongly suggests that our gold standard is accurate. Meanwhile, for a given sampling density, the errors occurring with the SL phantom are consistently larger than the ones corresponding to the brain phantom. This is explained by the fact that the SL phantom presents edge transitions of larger intensity.

C. Applications

1) Investigation of Aliasing Artifacts: Let us consider the function $f(\mathbf{u}) = S\rho(\mathbf{Mu})$ which depends on the spatial sampling step matrix $\mathbf{M}$. According to (1), the analytical MR data are given by $m_S(\mathbf{k}) = |\mathbf{M}|\hat{f}(-\mathbf{Mk})$.

When the benefits of an analytical model are forsaken, the MRI data are generated from a rasterized version of the phantom and the sensitivity, using the (nonnecessarily uniform) discrete Fourier transform (DFT)

$$m_{\mathbf{M}}(\mathbf{k}) = |\mathbf{M}|F\left(\mathrm{e}^{-2\pi\mathrm{j}\mathbf{Mk}}\right) \tag{31}$$

with $\|\mathbf{Mk}\|_\infty \le 1/2$ and

$$F\left(\mathrm{e}^{2\mathrm{j}\pi\boldsymbol{\nu}}\right) = \sum_{\mathbf{p}\in\mathbb{Z}^2} f(\mathbf{p})\mathrm{e}^{-2\mathrm{j}\pi\mathbf{p}\cdot\boldsymbol{\nu}} = \sum_{\mathbf{q}\in\mathbb{Z}^2} \hat{f}(\boldsymbol{\nu}+\mathbf{q}). \tag{32}$$

The right-hand side of (32) can be worked out using Poisson's summation formula. The terms with $\mathbf{q} \ne \mathbf{0}$ represent the aliasing that occurs with rasterized simulations. Due to the intrinsically discontinuous nature of the phantom ρ, the Fourier transform $\hat{f}$ decreases slowly, leading to significant aliasing artifacts. However, as the sampling density increases $(\mathrm{Tr}(\mathbf{M}) \to 0)$, the impact of aliasing is reduced, as we saw in Section IV-B.

Let us define an ideal anti-aliasing filter h in the Fourier domain as

$$\hat{h}(\boldsymbol{\nu}) = \begin{cases} 1, & \text{if } \|\boldsymbol{\nu}\|_\infty \le 1/2 \\ 0, & \text{otherwise.} \end{cases} \tag{33}$$

For normalized frequencies $\boldsymbol{\nu}$ such that $\|\boldsymbol{\nu}\|_\infty \le 1/2$, the analytical simulation (unaliased) is characterized as the DFT of the samples of the low pass-filtered continuous signal

$$\hat{f}(\boldsymbol{\nu}) = \sum_{\mathbf{p}\in\mathbb{Z}^2} (h * f)(\mathbf{p})\mathrm{e}^{-2\mathrm{j}\pi\mathbf{p}\cdot\boldsymbol{\nu}} \tag{34}$$

where $(h * f)$ represents the spatial continuous convolution of h and f.

When using a full Cartesian k-space sampling, the classical approach to reconstruction is to perform an inverse DFT. In this case, the samples of the signal f will be perfectly recovered out of the rasterized simulation (32) which is not desired because it conceals the existence of the Gibbs phenomenon due to the antialiasing filter (see, for instance, [18]). By contrast, the data provided by our analytical model lead to a fairer reconstruction where the Gibbs phenomenon appears. This effect is illustrated in Fig. 6.

Counterintuitively, the reconstructions out of rasterized simulations lead to aliasing effects that have a *positive* impact on visual quality. This situation, which occurs when the same model is used for both simulation and reconstruction, is sometimes referred to as "inverse crime." It arises because of the artificially imposed consistency between the computational forward models used for simulation and reconstruction. In such an inverse-crime situation, the continuous nature of the underlying physical model is not taken into account.

2) Impact of Rasterized Simulations on Reconstruction: We consider a plausible pMRI setup. It involves an array of eight receiver coils that are uniformly distributed around the phantom. The corresponding sensitivity maps are computed according to Biot–Savart's law. Spiral and EPI k-space trajectories are considered, both supporting a 256×256 image with reduction factor $R = 4$. The simulated raw data are generated using our analytical method as well as 256×256 and 512×512 rasterized simulations (see Section IV-C1). The same realization of complex Gaussian noise is added to the simulated data with different intensities, according to three scenarios: very low noise (40 dB SNR), normal data (30 dB SNR), and very noisy data (20 dB SNR). Reconstructions are performed using quadratic (Tikhonov linear solution) and TV regularizations. The reconstruction algorithms use the same forward model, in the form of the same encoding matrix $\mathbf{E}$. The experiments only differ in terms of the input data. The regularization parameter is tuned to optimize the signal-to-error
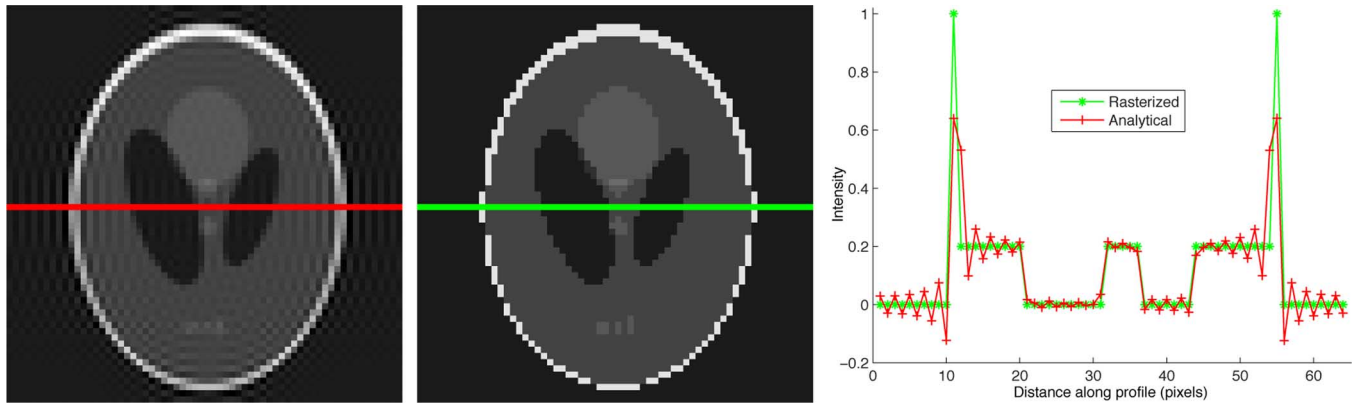
Fig. 6. 64×64 SL full Cartesian sampling reconstructions. From left to right: analytical simulation, rasterized "inverse crime" simulation, and corresponding line profiles.
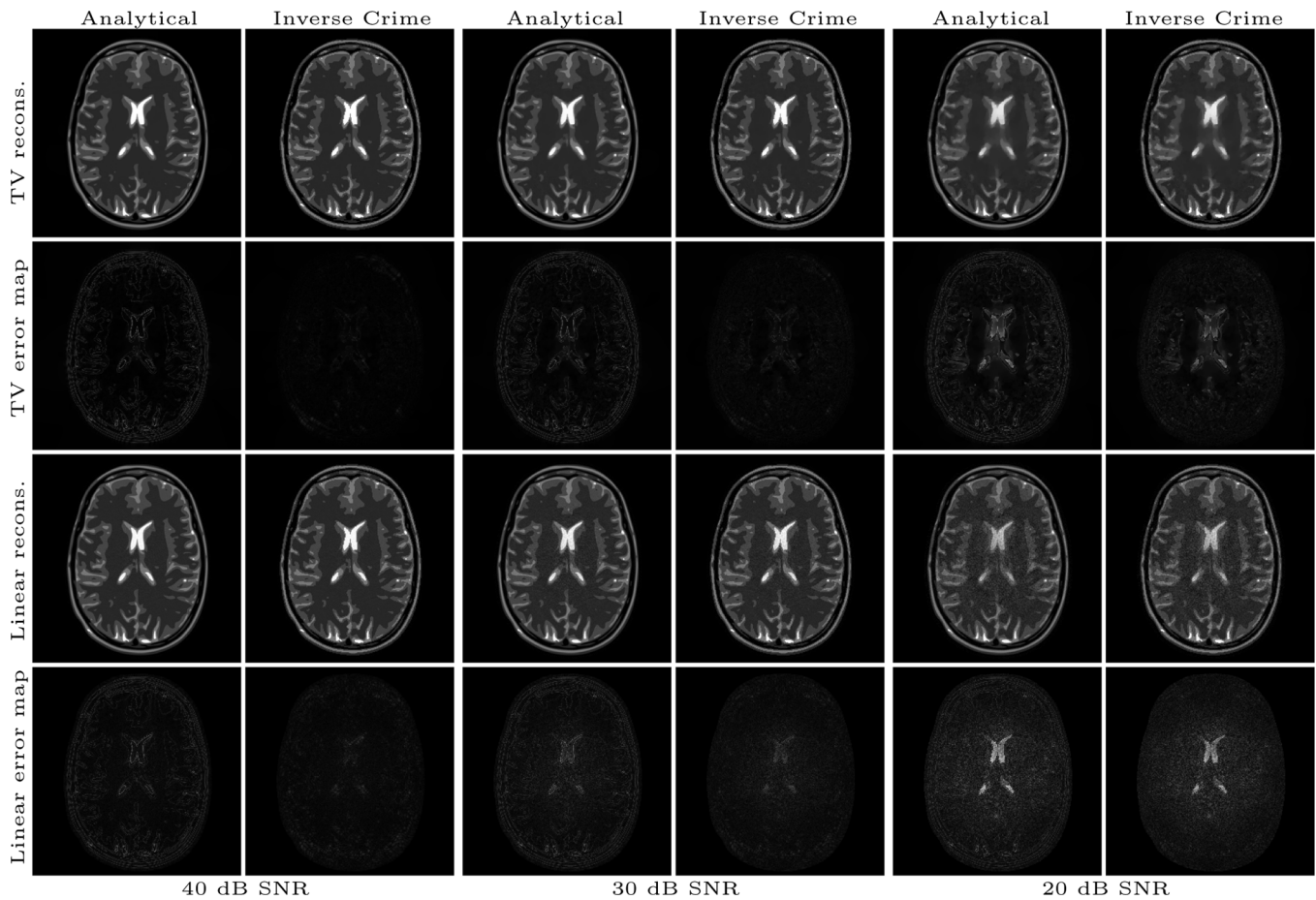

Fig. 7. Reconstructed brain phantoms and error maps for the spiral SENSE experiment.

ratio (SER) with respect to the ground-truth phantom (256×256 rasterization of the phantom). We report our results in Table VII for the spiral trajectory and in Table VIII for the EPI experiments. Reconstructed images are shown in Figs. 7 and 8, together with their error maps, in order to illustrate the impact of the inverse-crime situation (the 256×256 rasterized simulation) in the different scenarios.

The reconstructions in the spiral experiment are penalized compared to the EPI ones, in the sense that the high-frequency corners of the k-space are not sampled which leads to slightly inferior resolution. This explains that, all other parameters remaining constant, the EPI reconstructions outperform the spiral ones qualitatively and quantitatively.

We observe that the reconstructions from rasterized simulations consistently outperform the ones obtained from analytical measurements. While large differences can occur between the inverse-crime scenario (the 256×256 rasterized simulations) and the analytical simulation data, the 512×512 simulations yield much closer performance, with at most a 0.6 dB SER difference. This is explained by the reduced aliasing artifacts when
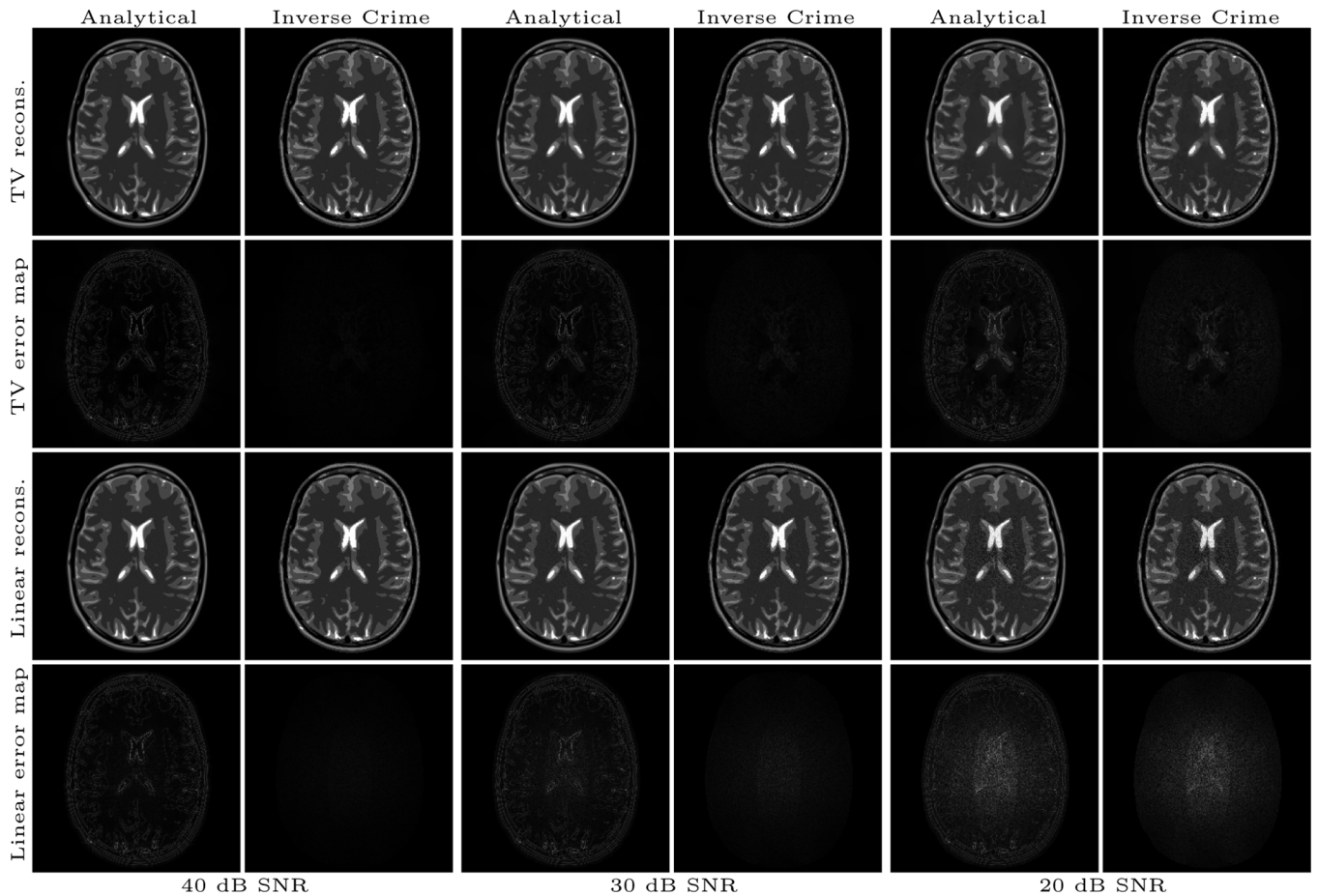
Fig. 8. Reconstructed brain phantoms and error maps for the EPI SENSE experiment.

TABLE VII
RECONSTRUCTION BIAS OF RASTERIZED SIMULATIONS ON QUADRATIC AND TV REGULARIZATION RECONSTRUCTIONS OF THE BRAIN PHANTOM FOR THE SPIRAL SENSE EXPERIMENT. OPTIMIZED SER AND CORRESPONDING BIAS ARE SHOWN IN dB

| Channel data SNR | | 40dB | | 30dB | | 20dB | |
Sampling density		256	512	256	512	256	512
Linear	SER	24.61	19.92	20.31	17.99	14.09	13.45
	Bias	5.07	0.37	2.56	0.24	0.75	0.11
TV	SER	33.75	20.80	27.60	20.26	19.61	17.72
	Bias	13.45	0.49	7.75	0.42	2.43	0.54

TABLE VIII
RECONSTRUCTION BIAS OF RASTERIZED SIMULATIONS ON QUADRATIC AND TV REGULARIZATION RECONSTRUCTIONS OF THE BRAIN PHANTOM FOR THE EPI SENSE EXPERIMENT. OPTIMIZED SER AND CORRESPONDING BIAS ARE SHOWN IN dB

| Channel data SNR | | 40dB | | 30dB | | 20dB | |
Sampling density		256	512	256	512	256	512
Linear	SER	36.25	20.77	26.30	19.79	16.73	15.31
	Bias	16.02	0.54	6.95	0.44	1.61	0.19
TV	SER	42.25	20.98	32.75	20.73	23.92	19.29
	Bias	21.85	0.58	12.57	0.55	5.02	0.39

doubling the sampling density (see Section IV-C1). As expected for this type of piecewise-constant phantom, the TV reconstructions consistently outperform the linear ones. Whatever the simulation method is, TV brings a significant improvement in the very noisy scenario. However, for the other scenarios (SNR 30 dB and 40 dB), the improvement over linear reconstruction is modest when using the analytic measurements, whereas it is artificially spectacular using the 256×256 rasterized simulations. We believe that our quality assessment, obtained analytically, offers fairer predictions of the practical worth of a reconstruction method than its overly optimistic rasterized version.

V. CONCLUSION

We proposed a method to develop realistic analytical phantoms for parallel MRI. Our analytical phantom approach offers strong advantages for the quantitative validation of MRI and pMRI reconstruction softwares: it is flexible enough to represent general imaging targets, it provides highly accurate representation of the physical continuous model and avoids overly optimistic reconstructions. This kind of framework is also applicable to the assessment of advanced MRI reconstruction methods such as autocalibrating parallel imaging, B0 correction [19], motion correction [20], [21], or higher order field imaging [22].

Implementations of the phantom are made available to the community.

APPENDIX

Proof of Theorem III-2: First, we consider the case $\boldsymbol{\omega} = \mathbf{0}$.

Proof: Take $\psi(\mathbf{r}) = \mathbf{r}^{\boldsymbol{\alpha}}$ and $\varphi(\mathbf{r}) = (\mathbf{e}_k \cdot \mathbf{r})^2/2 = r_k^2/2$. Then, $\boldsymbol{\nabla}(\mathbf{r}^{\boldsymbol{\alpha}}) \cdot \mathbf{e}_k = \alpha_k \mathbf{r}^{\boldsymbol{\alpha} - \mathbf{e}_k}$, $\boldsymbol{\nabla}\varphi = r_k \mathbf{e}_k$, and $\Delta\varphi = 1$. Using

Green's first identity yields $(1 + \alpha_k)f_{\mathcal{B}}^{\boldsymbol{\alpha}}(\mathbf{0}) = \int_{\partial \mathcal{B}} \mathbf{r}^{\boldsymbol{\alpha}+\mathbf{e}_k} \mathbf{e}_k \cdot \mathbf{n}\mathrm{d}\sigma$. ∎

For the case $\boldsymbol{\omega} \neq \mathbf{0}$, we need an intermediate result.

Lemma A1: For $\boldsymbol{\omega} \in \mathbb{R}^d \setminus \{\mathbf{0}\}$ and $\boldsymbol{\alpha} \in \mathbb{N}^d$

$$f_{\mathcal{B}}^{\boldsymbol{\alpha}}(\boldsymbol{\omega}) = \mathrm{j}g_{\mathcal{B}}^{\boldsymbol{\alpha}}(\boldsymbol{\omega}) + \sum_i \left(\frac{-\mathrm{j}\omega_i}{\|\boldsymbol{\omega}\|^2}\right) \alpha_i f_{\mathcal{B}}^{\boldsymbol{\alpha}-\mathbf{e}_i}(\boldsymbol{\omega}). \tag{35}$$

Proof: Use Green's first identity with $\psi(\mathbf{r}) = \mathbf{r}^{\boldsymbol{\alpha}}$, $\varphi(\mathbf{r}) = -\mathrm{e}^{-\mathrm{j}\boldsymbol{\omega}\cdot\mathbf{r}}$, and the fact that $\mathbf{x} \cdot \boldsymbol{\nabla}\mathbf{r}^{\boldsymbol{\alpha}} = \sum_i x_i\alpha_i\mathbf{r}^{\boldsymbol{\alpha}-\mathbf{e}_i}$. ∎

Let us continue the proof of Theorem III-2 by mathematical induction on $n = |\boldsymbol{\alpha}|$. For $n = 0$, $\boldsymbol{\alpha} = \mathbf{0}$ and the result holds true according to Lemma A1. When considering $n = 1$, $\boldsymbol{\alpha} = \mathbf{e}_i$, and Lemma A1, we obtain $f_{\mathcal{B}}^{\mathbf{e}_i}(\boldsymbol{\omega}) = \mathrm{j}g_{\mathcal{B}}^{\mathbf{e}_i}(\boldsymbol{\omega}) + \omega_i/\|\boldsymbol{\omega}\|^2 g_{\mathcal{B}}^{\mathbf{0}}(\boldsymbol{\omega})$. This is true for all i, hence the result holds true for $n = 1$. Now, we suppose the result holds true at order n and we consider $\boldsymbol{\alpha}$ such that $|\boldsymbol{\alpha}| = n+1$. From Lemma A1, we have that $f_{\mathcal{B}}^{\boldsymbol{\alpha}}(\boldsymbol{\omega}) = \mathrm{j}g_{\mathcal{B}}^{\boldsymbol{\alpha}}(\boldsymbol{\omega}) + \sum_i \left(-\mathrm{j}\omega_i/\|\boldsymbol{\omega}\|^2\right) \alpha_i f_{\mathcal{B}}^{\boldsymbol{\alpha}-\mathbf{e}_i}(\boldsymbol{\omega})$. Since $|\boldsymbol{\alpha} - \mathbf{e}_i| = n$, we substitute $f_{\mathcal{B}}^{\boldsymbol{\alpha}-\mathbf{e}_i}$ using the induction hypothesis and, after simplifications, we obtain

$$f_{\mathcal{B}}^{\boldsymbol{\alpha}}(\boldsymbol{\omega}) = \mathrm{j}g_{\mathcal{B}}^{\boldsymbol{\alpha}}(\boldsymbol{\omega}) + \mathrm{j}\sum_i \sum_{\mathbf{m}=\mathbf{0}}^{\boldsymbol{\alpha}} \left(\frac{-\mathrm{j}\boldsymbol{\omega}}{\|\boldsymbol{\omega}\|^2}\right)^{\boldsymbol{\alpha}-\mathbf{m}}$$
$$\times |\boldsymbol{\alpha} - \mathbf{m}|!d_i(\boldsymbol{\alpha} - \mathbf{m})\binom{\boldsymbol{\alpha}}{\mathbf{m}}g_{\mathcal{B}}^{\mathbf{m}}(\boldsymbol{\omega})$$

with $d_i(\mathbf{x}) = x_i/|\mathbf{x}|$ for $\mathbf{x} \neq \mathbf{0}$ and $d_i(\mathbf{0}) = 0$. By permutation of the sums and noting that $\sum_i d_i(\mathbf{x}) = 1$ for $\mathbf{x} \neq \mathbf{0}$ and $\sum_i d_i(\mathbf{0}) = 0$, we get

$$f_{\mathcal{B}}^{\boldsymbol{\alpha}}(\boldsymbol{\omega}) = \mathrm{j}\sum_{\mathbf{m}=\mathbf{0}}^{\boldsymbol{\alpha}} \left(\frac{-\mathrm{j}\boldsymbol{\omega}}{\|\boldsymbol{\omega}\|^2}\right)^{\boldsymbol{\alpha}-\mathbf{m}} |\boldsymbol{\alpha} - \mathbf{m}|!\binom{\boldsymbol{\alpha}}{\mathbf{m}}g_{\mathcal{B}}^{\mathbf{m}}(\boldsymbol{\omega}).$$

This is valid for all $\boldsymbol{\alpha}$ such that $|\boldsymbol{\alpha}| = n+1$. Hence, the induction hypothesis was proved at order $n + 1$ assuming it holds true at order n.

Characterization and Computations of a Family of 1-D Integrals:

Proposition A-2: For $m \in \mathbb{N}$, $h^{(m)}$ follows the recursion rule

$$2\mathrm{j}bh^{(m+1)}(a,b) + \mathrm{j}ah^{(m)}(a,b) - mh^{(m-1)}(a,b)$$
$$+\mathrm{e}^{-\mathrm{j}(a+b)} = \delta_m.$$

Proof: Integrate $\int_0^1 -\mathrm{j}(a + 2b\lambda)\lambda^m\mathrm{e}^{-\mathrm{j}\lambda(a+\lambda b)}\mathrm{d}\lambda$ by parts and identify $h^{(m+1)}$, $h^{(m)}$ and $h^{(m-1)}$ if $m > 0$. ∎

Corollary A-3: For small values of a and b, one can rely on the backward iteration starting form a higher order $M > m$ to get accurate results

- $\tilde{h}^{(M+1)}(a,b) = \tilde{h}^{(M)}(a,b) = 0$
- $\tilde{h}^{(m)}(a,b) = 2\mathrm{j}b\tilde{h}^{(m+2)}(a,b) + \mathrm{j}a\tilde{h}^{(m+1)}(a,b) + \mathrm{e}^{-\mathrm{j}(a+b)}/m + 1$.

Proposition A-4: For b nonzero and $m \geq 1$, the forward iteration is used

-

$$h^{(0)}(a,b) =$$
$$\sqrt{\pi}\mathrm{e}^{\mathrm{j}a^2/4b}/(2\sqrt{\mathrm{j}b})\left[\mathrm{erf}\left((a+2b)\sqrt{\mathrm{j}}/2\sqrt{b}\right) - \mathrm{erf}\left(a\sqrt{\mathrm{j}}/2\sqrt{b}\right)\right]$$

-

$$h^{(m+1)}(a,b) =$$
$$(mh^{(m-1)}(a,b) - \mathrm{j}ah^{(m)}(a,b) + \mathrm{e}^{-\mathrm{j}(a+b)})/(2\mathrm{j}b)$$

with $\mathrm{erf}(z) = 2z/\sqrt{\pi}\int_0^1 \mathrm{e}^{-z^2t^2}\mathrm{d}t$.

Proof: From Proposition A.2 with $m = 0$ and $b = 0$, we get $h^{(0)}(a,0) = \mathrm{e}^{-\mathrm{j}a/2}\mathrm{sinc}(a/(2\pi))$. In the case $b \neq 0$, we define $t = \lambda + a/2b$ such that $\lambda(a + b\lambda) = a^2/4b - bt^2$. By Definition (23), we get $\mathrm{e}^{-\mathrm{j}a^2/4b}\int_0^1 \mathrm{e}^{-\mathrm{j}bt^2}\mathrm{d}\lambda$. By a change of variable and splitting the integral, we obtain $\mathrm{e}^{\mathrm{j}a^2/4b}\left(\int_0^{a/2b+1} \mathrm{e}^{-\mathrm{j}bt^2}\mathrm{d}t - \int_0^{a/2b} \mathrm{e}^{-\mathrm{j}bt^2}\mathrm{d}t\right)$. The result follows from normalizing the integration intervals. ∎

Proposition A-5: For b small, the truncated Taylor series in $b = 0$ provides accurate results

$$h^{(m)}(a,b) = \sum_{n=0}^{\infty} \frac{(-\mathrm{j}b)^n\gamma(m + 2n + 1, \mathrm{j}a)}{n!(\mathrm{j}a)^{m+2n+1}} \tag{36}$$

where the lower incomplete gamma function is defined as $\gamma(s,z) = z^s\int_0^1 \lambda^{s-1}\mathrm{e}^{-\lambda z}\mathrm{d}\lambda$.

Proof: Note that $\mathrm{e}^{-\mathrm{j}\lambda(a+\lambda b)} = \mathrm{e}^{-\mathrm{j}\lambda a}\sum_{n=0}^{\infty}(-\mathrm{j}\lambda^2 b)^n/n!$. By virtue of Fubini's theorem, we get

$$h^{(m)}(a,b) = \sum_{n=0}^{\infty}(-\mathrm{j}b)^n h^{(m+2n)}(a,0)/n!.$$

Identify $\gamma(m + 2n + 1, \mathrm{j}a)$ to $(\mathrm{j}a)^{m+2n+1}h^{(m+2n)}(a,0)$. ∎

Proof of Proposition III-4:

Proof: We rewrite $g_{\mathcal{B}}^{\boldsymbol{\alpha}}$ using Characterization (22) with $F(\mathbf{r}) = \mathbf{r}^{\boldsymbol{\alpha}}\mathrm{e}^{-\mathrm{j}\boldsymbol{\omega}\cdot\mathbf{r}}/\|\boldsymbol{\omega}\|^2\boldsymbol{\omega}$ for $\boldsymbol{\omega} \neq \mathbf{0}$ and $F(\mathbf{r}) = \mathbf{r}^{\boldsymbol{\alpha}+\mathbf{e}_k}/(1 + \alpha_k)\mathbf{e}_k$ for $\boldsymbol{\omega} = \mathbf{0}$. The piecewise parameterization of the contour (Table III) is then used, and by virtue of the multinomial theorem, we expand the terms $\mathbf{r}^{\boldsymbol{\alpha}}$ and $\mathbf{r}^{\boldsymbol{\alpha}+\mathbf{e}_k}$. ∎

REFERENCES

[1] F. I. Karahanoğlu, D. Van De Ville, K. Pruessmann, and M. Unser, "Analytical form of Shepp-Logan phantom for parallel MRI," in *Proc. ISBI*, Rotterdam, The Netherlands, Apr. 14–17, 2010, pp. 261–264.
[2] A. Ribés and F. Schmitt, "Linear inverse problems in imaging," *IEEE Signal Process. Mag.*, vol. 25, no. 4, pp. 84–99, Jul. 2008.
[3] L. Shepp and B. Logan, "The Fourier reconstruction of a head section," *IEEE Trans. Nucl. Sci.*, vol. 21, pp. 21–43, Jun. 1974.
[4] M. Smith *et al.*, "Alternatives to the use of the DFT in MRI and spectroscopic reconstructions," *Int. J. Imag. Syst. Technol.*, vol. 8, no. 6, pp. 558–564, Dec. 1997.
[5] R. Van de Walle *et al.*, "Reconstruction of MR images from data acquired on a general nonregular grid by pseudoinverse calculation," *IEEE Trans. Med. Imag.*, vol. 19, no. 12, pp. 1160–1167, Dec. 2000.
[6] C. Koay, J. Sarlls, and E. Ãzarslan, "Three-dimensional analytical magnetic resonance imaging phantom in the Fourier domain," *Magn. Reson. Med.*, vol. 58, no. 2, pp. 430–436, Aug. 2007.

[7] H. Gach, C. Tanase, and F. Boada, "2D & 3D Shepp-Logan phantom standards for MRI," in *Proc. 19th Int. Conf. Syst. Eng.*, Los Alamitos, CA, Aug. 19–21, 2008, pp. 521–526.

[8] L. Greengard and C. Stucchio, "Spectral edge detection in two dimensions using wavefronts," *Appl. Computat. Harmonic Anal.*, vol. 30, no. 1, pp. 69–95, 2011.

[9] T. M. Ngo, G. S. Fung, B. M. Tsui, E. McVeigh, and D. A. Herzka, "Three dimensional digital polyhedral phantom framework with analytical Fourier transform and application in cardiac imaging," in *Proc. ISMRM*, 2011, pp. 1310–1310.

[10] K. P. Pruessmann, M. Weiger, M. Scheidegger, and P. Boesiger, "SENSE: Sensitivity encoding for fast MRI," *Magn. Reson. Med.*, vol. 42, no. 5, pp. 952–962, Oct. 1999.

[11] W. Segars, D. Lalush, and B. Tsui, "A realistic spline-based dynamic heart phantom," *IEEE Trans. Nucl. Sci.*, vol. 46, no. 3, pp. 503–506, Jun. 1999.

[12] S. Vembu, "Fourier transformation of the n-dimensional radial delta function," *Q. J. Math.*, vol. 12, no. 1, pp. 165–168, 1961.

[13] E. Sorets, "Fast Fourier transforms of piecewise constant functions," *J. Computat. Phys.*, vol. 116, no. 2, pp. 369–379, 1995.

[14] M. Jacob, T. Blu, and M. Unser, "An exact method for computing the area moments of wavelet and spline curves," *IEEE Trans. Pattern Anal. Mach. Intell.*, vol. 23, no. 6, pp. 633–642, Jun. 2001.

[15] W. Gautschi, "Computational aspects of three-term recurrence relations," *SIAM Rev.*, vol. 9, pp. 24–82, Jan. 1967.

[16] D. Geman and C. Yang, "Nonlinear image recovery with half-quadratic regularization," *IEEE Trans. Image Process.*, vol. 4, no. 7, pp. 932–946, Jul. 1995.

[17] F. Champagnat and J. Idier, "A connection between half-quadratic criteria and EM algorithms," *IEEE Signal Process. Lett.*, vol. 11, no. 9, pp. 709–712, Sep. 2004.

[18] R. Archibald and A. Gelb, "A method to reduce the Gibbs ringing artifact in MRI scans while keeping tissue boundary integrity," *IEEE Trans. Med. Imag.*, vol. 21, no. 4, pp. 305–319, Apr. 2002.

[19] L. Man, J. Pauly, and A. Macovski, "Multifrequency interpolation for fast off-resonance correction," *Magn. Reson. Med.*, vol. 37, no. 5, pp. 785–792, Apr. 1997.

[20] M. Zaitsev, C. Dold, G. Sakas, J. Hennig, and O. Speck, "Magnetic resonance imaging of freely moving objects: Prospective real-time motion correction using an external optical motion tracking system," *NeuroImage*, vol. 31, no. 3, pp. 1038–1050, 2006.

[21] M. B. Ooi, S. Krueger, W. J. Thomas, S. V. Swaminathan, and T. R. Brown, "Prospective real-time correction for arbitrary head motion using active markers," *Magn. Reson. Med.*, vol. 62, no. 4, pp. 943–954, 2009.

[22] B. J. Wilm, C. Barmet, M. Pavan, and K. P. Pruessmann, "Higher order reconstruction for MRI in the presence of spatiotemporal field perturbations," *Magn. Reson. Med.*, vol. 65, no. 6, pp. 1690–1701, 2011.